



CHORUS

This is the accepted manuscript made available via CHORUS. The article has been published as:

Lattice-level observation of the elastic-to-plastic relaxation process with subnanosecond resolution in shock-compressed Ta using time-resolved in situ Laue diffraction

C. E. Wehrenberg, A. J. Comley, N. R. Barton, F. Coppari, D. Fratanduono, C. M. Huntington, B. R. Maddox, H.-S. Park, C. Plechaty, S. T. Prsbrey, B. A. Remington, and R. E. Rudd

Phys. Rev. B **92**, 104305 — Published 29 September 2015

DOI: [10.1103/PhysRevB.92.104305](https://doi.org/10.1103/PhysRevB.92.104305)

Lattice-level observation of the elastic-to-plastic relaxation process with sub-nanosecond resolution in shock compressed Ta using time-resolved *in-situ* Laue diffraction

C. E. Wehrenberg,¹ A. J. Comley,² N. R. Barton,¹ F. Coppari,¹ D. Fratanduono,¹ C. M. Huntington,¹ B. R. Maddox,¹ H.-S. Park,¹ C. Plechaty,³ S. T. Prisbrey,¹ B. A. Remington,¹ and R. E. Rudd¹

¹*Lawrence Livermore National Laboratory, Livermore, CA, 94550, USA*

²*Atomic Weapons Establishment, Aldermaston, Reading RG7 4PR, United Kingdom*

³*Riverside Research, Beavercreek, OH 45431, USA*

We report direct lattice level measurements of plastic relaxation kinetics through time-resolved, *in-situ* Laue diffraction of shock-compressed single-crystal [001] Ta at pressures of 27-210 GPa. For a 50 GPa shock, a range of shear strains is observed extending up to the uniaxial limit for early data points (<0.6 ns) and the average shear strain relaxes to a near steady state over ~ 1 ns. For 80 and 125 GPa shocks, the measured shear strains are fully relaxed already at 200 ps, consistent with rapid relaxation associated with the predicted threshold for homogeneous nucleation of dislocations occurring at shock pressure ~ 65 GPa. The relaxation rate and shear stresses are used to estimate the dislocation density and these quantities are compared to the results of other high pressure work, flow stress models, and molecular dynamics simulations.

PACS numbers: 62.20.F-, 61.05.cp, 62.50.Ef, 62.50.-p

I. INTRODUCTION

Shocks are ubiquitous in nature, yet when shock waves propagate into solids, a full understanding of the response of the solid is still lacking. Shock waves have traditionally been studied by velocimetry techniques, measuring the speed and amplitude of the elastic and plastic waves. Such techniques, however, do not probe the elastic to plastic transition at the lattice level, and provide little understanding of the underlying lattice relaxation kinetics. In many cases, the flow stress (the sample resistance to plastic deformation) associated with a shock wave has been viewed as equivalent to the Hugoniot (shock wave) elastic limit, even though the flow stress may change over time after exceeding the elastic limit¹. This view is reflected in a wide variety of engineering models that treat the flow stress as a static quantity, the “strength,” notionally equivalent to the yield strength that is familiar from quasi-static loading tests. In these models the strength is a function of the pressure, temperature, plastic strain or strain rate, with no direct tie to the lattice defects, such as dislocations, that actually create the plastic flow.

In-situ time resolved diffraction provides a direct observation of the lattice level response where these defects responsible for plastic deformation reside and evolve. X-ray diffraction has proven to be an effective tool for studying crystal structure but has been challenging to implement for shock kinetics due to signal-to-noise and temporal-resolution issues in ultra-short time experiments. Recently, advanced synchrotron sources have been used to overcome these issues, but are limited to polycrystalline samples and in the range of available loading pressures². The technique we report here combines time-resolved Laue diffraction with laser-driven shock loading over a wide range of pressure, allowing us to observe plastic re-

laxation kinetics in single-crystals directly at the lattice level as a function of time. In doing so, we move beyond the common practice of considering the post-shock Hugoniot conditions as a well-defined thermodynamic state to considering the detailed kinetics of how that state is reached. The plasticity then is not just rate dependent, but time dependent. The latest flow stress models, such as the Livermore Multiscale Strength (LMS) model³, predict the flow stress as a function of time from the evolution of the dislocation density, ρ_d , and dislocation velocity, v_d , not just the current thermodynamic state variables (pressure, temperature, etc.). The LMS model in particular predicts that a material under shock loading has a flow stress that evolves with time under constant post-shock conditions over the short time scales accessed in the experiment. Previous dynamic diffraction experiments of shocked Ta with ~ 100 GPa shocks observed no time dependence in the measured flow stress behind the shock. These strong shocks were above the theoretical threshold, $P_{thresh} \sim 65$ GPa, for homogeneous nucleation of dislocations⁴⁻⁶, where the predicted lattice relaxation time is < 10 ps, which is far below the 150 ps experimental time resolution of our technique. Here we present dynamic Laue diffraction experiments on shocked single-crystal Ta that span shock strengths from 27 - 210 GPa, to measure the differences in the lattice plastic relaxation response as the shock strength is increased from below to above $P_{thresh} \sim 65$ GPa.

II. EXPERIMENTAL TECHNIQUE

The diffraction experiments were performed at the OMEGA laser facility using the Broadband X-Ray Diffraction (BBXRD) diagnostic and an imploding CH capsule as the x-ray source. The experimental setup is

shown in Fig. 1 and has been described previously^{4,7,8}. A set of 29-42 beams was used to drive an implosion in a hollow plastic capsule with 980 μm diameter and a 9 μm thick wall to produce a bright, short (~ 150 ps) burst of broadband x-rays (5-25 keV) generated by bremsstrahlung radiation when the capsule material stagnates at the center^{7,8}. A planar shock wave is created in the Ta crystal by direct laser illumination using a single 3ω beam with a distributed phase plate to smooth the spot profile and a 1-4 ns square pulse shape. The targets consisted of an ablator, either 10 μm thick nanocrystalline diamond or 350 μm thick polystyrene (CH), glued to 4-6 μm thick single-crystal Ta, and a tamper, attached either with glue, for microcrystalline diamond tampers, or gluelessly, for MgO tampers⁸. Figure 2 shows example traces for Velocity Interferometer System for Any Reflector (VISAR)⁹ from shots using the two types of ablaters. The VISAR trace, showing the Ta/tamper interface velocity, for the diamond ablator shows a rise and fall in velocity, corresponding to reverberations arising from impedance differences in the diamond, tantalum, and glue layers⁶. The CH ablator is essentially impedance-matched to the glue layer, creating a flat top VISAR trace that corresponds to a steady shock. Despite the differences in the drive histories, comparisons of shots taken at similar pressures and times show general agreement. It should be noted that the rise time of the shock wave (~ 400 ps) is somewhat faster than the rise time of velocity traces (~ 600 ps) shown for drive (A), the CH ablator drive, due to the long etalon delay used for those shots.

The longitudinal stress created in the sample was determined by impedance matching using both the peak velocity as measured by VISAR and from laser-intensity scaling¹⁰, with the two methods agreeing within 8% on average. In previous analyses of the VISAR data from laser-driven shocks, a correction factor of 2.7 was used for diamond windows based on diamond anvil cell data⁴. Recent data from high-rate ramp-compression of diamond on the National Ignition Facility lead to a correction factor of 1.95 ± 0.05 ¹¹ (The MgO correction factor is 1.78¹²). Using the new value improves the agreement between the two stress measurements and significantly reduces the experimental uncertainty.

Figure 3 shows a Laue pattern recorded from a Ta single-crystal shock compressed to 64 ± 7 GPa. Diffraction spots are observed simultaneously from both the undriven and driven lattice. For the geometry used here, the driven spots (marked with a red \square) will appear above the ambient spots (green \circ) when under compression. The shape of the undriven signal corresponds to elliptical $\sim 550 \times 300$ μm x-ray source created during the stagnation phase of the asymmetrical capsule implosion⁸. A halo signal can be seen around some of the undriven spots, caused by the low-intensity, ~ 1 mm x-ray source that arises during the early implosion stages from the laser ablation. Shot-to-shot variations in the implosion can vary the shape and intensity of the halo. The orien-

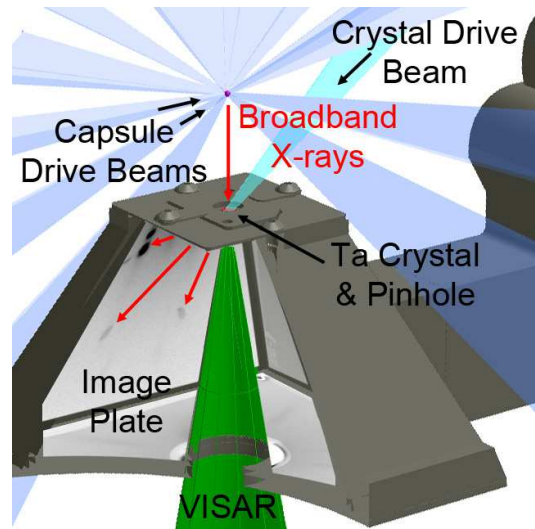


FIG. 1. Geometry of the experimental setup. A broadband x-ray spectrum is created by a CH capsule implosion driven by 29-42 beams. A separate beam is used to drive a shock wave into the Ta crystal target package. The shock drive is monitored on the back (non-drive) side by VISAR. Diffracted x-rays are recorded inside the BBXRD using image plates.

tation of the ambient crystal relative to BBXRD and the x-ray source is determined by fitting the undriven Laue spots. The driven spots can then be fit using a single parameter, the unit cell aspect ratio $\alpha = c/a$, where c and a are the unit cell dimensions along, and transverse to, the shock propagation direction, respectively. As shown by the sketch in Fig. 3, the diffracting plane changes orientation as the aspect ratio changes under compression, causing a shift in the diffraction spot position. Note that, for this setup, hydrostatic strain will not change the orientation of the planes, so that no shift in the position of the Laue spots will occur. The Laue data are sensitive only to shear strain, with lower aspect ratios corresponding to higher shear strain. A halo signal can be seen around some of the undriven spots, caused by the low-intensity, ~ 1 mm x-ray source that arises during the early implosion stages from the laser ablation. Shot-to-shot variations in the implosion can vary the shape and intensity of the halo. The orientation of the ambient crystal relative to BBXRD and the x-ray source is determined by fitting the undriven Laue spots. The driven spots can then be fit using a single parameter, the unit cell aspect ratio $\alpha = c/a$, where c and a are the unit cell dimensions along, and transverse to, the shock propagation direction, respectively. As shown by the sketch in Fig. 3, the diffracting plane changes orientation as the aspect ratio changes under compression, causing a shift in the diffraction spot position. Note that, for this setup, hydrostatic strain will not change the orientation of the planes, so that no shift in the position of the Laue spots will occur. The Laue data are sensitive only to shear strain, with lower aspect ratios corresponding to higher

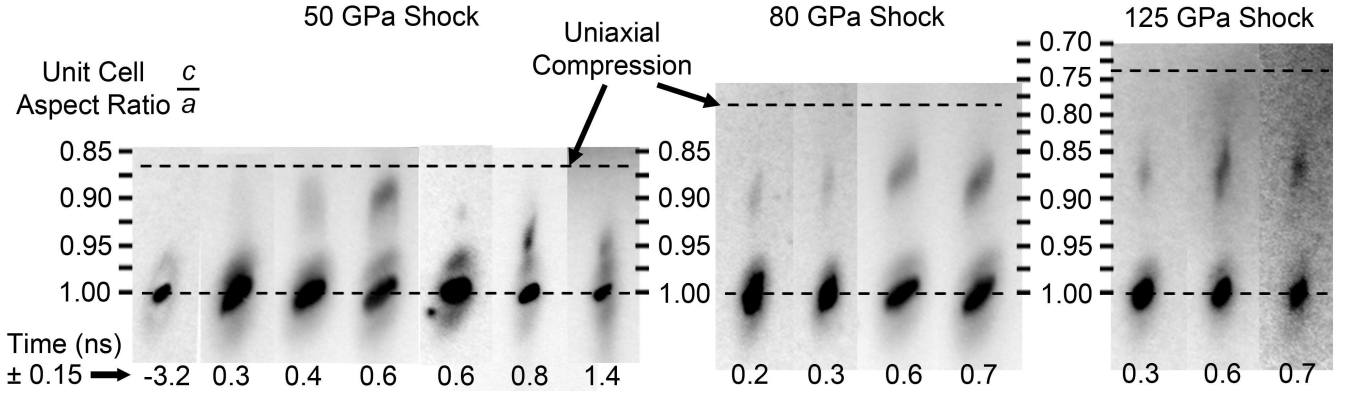


FIG. 4. Laue (211) diffraction spots for single-crystal Ta arranged in order (left to right) of increasing time relative to the arrival of a shock wave traveling along the [001] direction. Series are shown for shocks with pressure (mean stress) of $P_{shk} = 50, 80,$ and $125 \text{ GPa} \pm 15\%$. The driven diffraction spots appear above the undriven spots and, after adjusting for orientation differences, the distance between the spots is a function of the unit cell aspect ratio. Dotted lines indicated the positions of the undriven spots and the expected location of driven spots when under uniaxial 1D elastic compression.

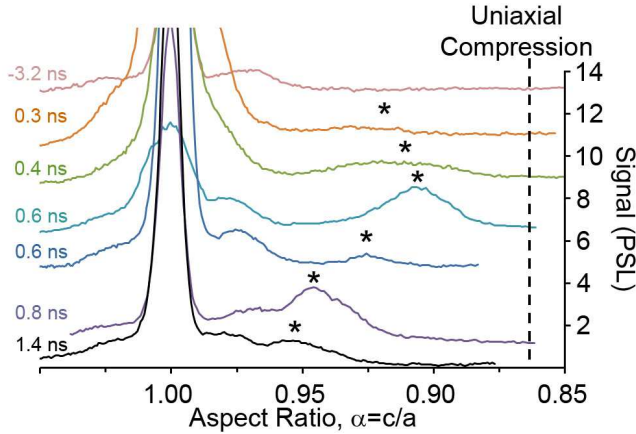


FIG. 5. Lineouts through the driven and undriven diffraction spots, plotted versus cell aspect ratio, $\alpha = c/a$, giving a time series for a 50 GPa shock. The centroids of the driven spots are marked with asterisks. Lineouts have been shifted along the y-axis for clarity. The expected position for uniaxial 1D elastic compression is marked with a dashed line, and the tails of the earliest diffraction spots extend to this line.

faster than the resolution of the experiment ($\sim 0.15 \text{ ns}$). MD simulations using Model Generalized Pseudopotential Theory (MGPT) potential indicate that for $P_{shk} > 65 \text{ GPa}$ dislocations can homogeneously nucleate throughout the material, instead of multiplying from existing dislocations⁵. Homogeneous nucleation rapidly creates a large number of dislocations leading to a fast timescale for relaxation, $\tau_{1D-3D} < 10 \text{ ps}$. While these timescales are too short to be observed with the current Laue technique, the observed relaxation behavior is consistent with the predicted relaxation times. Alternatively, the fast relaxation times may indicate the onset of a high volume fraction of twinning, which some MD simulations using other interatomic potentials predict^{14,15}.

The shear stress, calculated using the aspect ratios measured from Fig. 4, is plotted versus time in Fig. 6 (A). Following Comley et al.⁴, the strains in the transverse and shock directions are

$$\varepsilon_T = 1 - (\alpha\eta_H)^{-1/3} \quad (1)$$

$$\varepsilon_S = 1 - (\alpha^2/\eta_H)^{1/3} \quad (2)$$

$$\bar{\sigma} = 2C'(P, T)(\varepsilon_S - \varepsilon_T) \quad (3)$$

where pressure measured from the combination of ablation scaling and VISAR is used to calculate the compression η_H on the Hugoniot. The effective shear modulus is $C' = 78 \pm 8 \text{ GPa}$ at $P_{shk} = 50 \pm 6 \text{ GPa}$ for $T(P_{shk}) = 630 \pm 50 \text{ K}$ on the Hugoniot. Since the shear strain is time dependent, a range of strains and stresses is present in the driven state. To provide an estimate of the total range of stresses, we use a 3σ range of strains from Gaussian fits to the spot profiles (grey boxes), while the error bars correspond to the average shear stress using the spot centers. The large 3σ range in the early data reflects a summation of x-ray signal from material in the shock front, uniaxial compressed, and relaxed states. Later in time the 3σ range narrows as the shock moves farther into the sample, since only a small fraction of driven material is in the shock front or uniaxial compression state. The predicted shear stress, calculated using the hydrocode ARES¹⁶ and the LMS model³, is plotted for a depth of $3 \mu\text{m}$ into the Ta. A Taylor factor of $M=2.45$ was used to represent the [001] single-crystal loading, and the Orowan parameter η is set to 2, consistent with the expected contribution of edge dislocations and with a separate series of Raleigh-Taylor instability experiments^{17,18}. Curves are shown for initial dislocation densities of 10^7 cm^{-2} (double line) and 10^9 cm^{-2} (single line), a likely range for high-quality single-crystals. An exact match is not expected since the hydrocode prediction follows a single point in the Ta, whereas the experimental measurement is volumetric through the $5 \mu\text{m}$

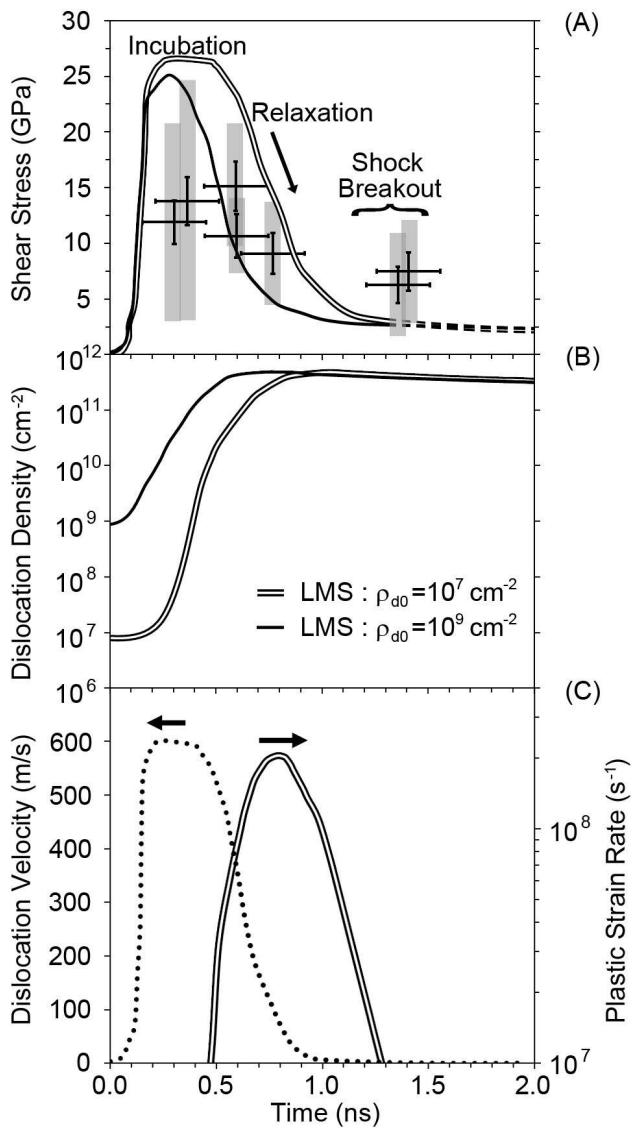


FIG. 6. (A) Von Mises shear stress versus time, calculated from dynamic Laue patterns for a series of 50 GPa shocked [001] Ta experiments, in comparison to the predicted shear stress from the LMS model³ at initial dislocation densities of 10^7 (double line) and 10^9 cm^{-2} (single line). Error bars indicate average shear stress while total stress ranges (grey boxes) are estimated using 3σ Gaussian fits to spot profiles. (B) The dislocation density predicted by the LMS model. (C) Dislocation velocity (left axis) and plastic strain rate (right axis) for the LMS model with 10^7 cm^{-2} initial dislocation density.

sample. In addition, the hydrocode simulation was done with the simplifying assumption of a pure shock from a flyer plate collision, whereas the laser-driven experiment may experience some x-ray preheat that is not captured by simulation. The model predicts a high initial shear stress near the uniaxial 1D compressive stress that relaxes asymptotically to a nearly steady flow stress over ~ 1 ns, approximately consistent with the experimental

data.

The relaxation behavior seen in Fig. 7 (A) can be understood using Orowan’s law.

$$\dot{\epsilon}_p = \frac{\rho_d b v_d \eta}{M} \quad (4)$$

where $\dot{\epsilon}_p$ is the plastic strain rate and b is the Burgers vector. The dislocation density from the LMS model is plotted in Fig. 6 (B) with initial values of $\rho_{d0} = 10^7 \text{ cm}^{-2}$ (double line) and $\rho_{d0} = 10^9 \text{ cm}^{-2}$ (single line), while the dislocation velocity (dotted line) and plastic strain rate (double line) are shown in Fig. 7 (C) for $\rho_{d0} = 10^7 \text{ cm}^{-2}$. The dislocation density is initially low, leading to low initial plastic strain rate so that the material response is nearly elastic (uniaxial compression). The shear stress is initially high as dislocations multiply and the dislocation density increases in an “incubation period” over the first ~ 0.5 ns. At this point the large density of dislocations creates a high plastic strain rate, rapidly relieving the high shear stress over the 0.5 - 1.0 ns interval in the “relaxation phase”, after which the lattice reaches a near steady relaxed state⁵. Notably, the dislocation density remains high after the relaxation phase, resulting in a residual shear stress via the Taylor hardening (work hardening). In the LMS model, the high residual dislocation density results from lower plastic strain rate in the relaxed state. As the shear stress is relaxed, the dislocation velocity falls and this slows down the strain rate and rate of dislocation annihilation.

Figure 7 (A) shows the shear stress measurements from all Laue shots, plotted versus shock pressure. Here, P_{shk} has shifted $\sim 30\%$ higher relative to the previous reports^{4,6} due to the improved VISAR correction factor discussed above. The large error bars at high pressure are dominated by uncertainty in the shear modulus due to a lack of high-pressure diamond anvil cell data above pressures of 100 GPa with which to compare the calculated elastic constants¹³. The data are divided into three categories based on the x-ray probe timing, 0.0-0.3 ns, 0.3-0.7 ns, and > 0.7 ns. For the 7 shots done at $P_{shk} \sim 50$ GPa, the shear stress increases somewhat initially as the shock enters the material, and then falls as lattice relaxation occurs. Figure 7 suggests a transition in relaxation mechanism near $P_{shk}=60$ -80 GPa. At pressures below this transition, the data show a wide range of shear stress due to the time dependent relaxation and the different times at which the data were taken. Above this transition, the data are time-independent over the timescale of the experiment.

IV. DISCUSSION

A. Other High-Pressure Strength Measurements

Diamond anvil cell experiments on tantalum indicate the yield strength generally increases with pressure, with

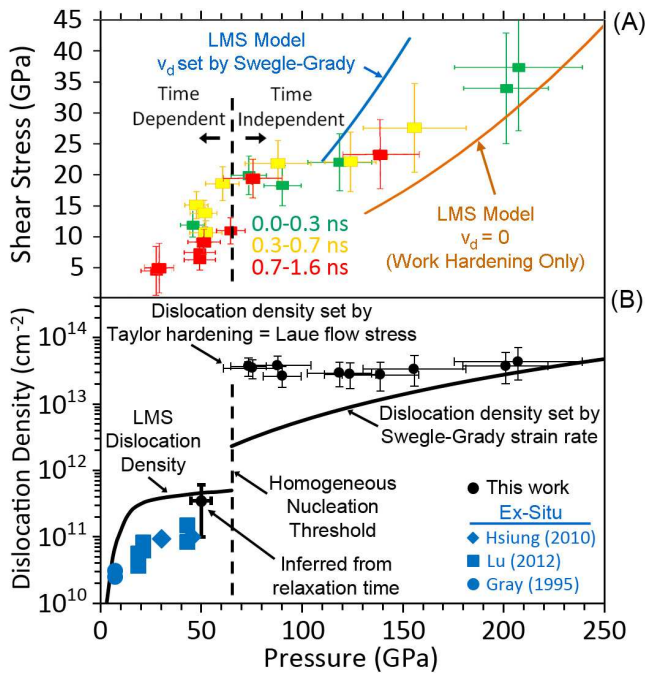


FIG. 7. (A) Shear stress versus shock pressure following the method of Comley et al.^{4,6}. The data are color coded according to the x-ray probe timing, green (0.0-0.3 ns), yellow (0.3-0.7 ns), and red (>0.7 ns). A transition between time-dependent ($P_{shk} < 0.7$ Mbar) and time-independent ($P_{shk} > 0.8$ Mbar) response is indicated. Two adaptations of the LMS model are shown representing the range of post-shock strain rates, from zero (orange curve) up to the strain rate in the shock front (blue curve) as estimated by the Swegle-Grady relationship. (B) Comparison of experimental dislocation density inferred from the relaxation time with *ex-situ* experimental studies and the LMS model. Above a shock strength of 65 GPa, data points indicate upper bounds estimated by equating Laue flow stress measurements to the Taylor hardening stress. Also shown is the LMS model saturation dislocation density for the Swegle-Grady strain rate.

single crystal samples reaching a yield strength of 4-5 GPa when under hydrostatic pressure of 100 GPa¹⁹. Softening behavior has been observed in polycrystalline samples in the 50-100 GPa pressure range^{20,21}. During uniaxial loading, Jing et al²¹ reported that the yield strength decreased $\sim 10\%$ as the pressure was increased from 50 to 70 GPa and then increased to 7 GPa under a pressure of 100 GPa. The authors attribute this softening behavior to a measured dip in the average microscopic deviatoric strain occurring in the same pressure range, but comment no further on the mechanism. It may be tempting to draw parallels between this softening behavior and the transition to fast relaxation found to occur at similar pressures in this work; however, the wide differences between the samples and strain rate make comparisons difficult.

The shear stresses measured in this work may be more appropriately compared to other high-strain-rate techniques, although most of the work for shock loading is

limited to the weak shock regime. Our measurements are several times higher than the 0.7-1.2 GPa shear stresses reported by Reed et al.¹ from wave-profile analysis of gas-gun driven shock compression of Ta to 25 GPa; however, the microsecond timescale of the gas-gun experiments means the material will have longer to relax and will have a much lower strain rate. Other gas-gun studies have reported higher shear stress for similar shock pressures. Glam et al.²² report a Hugoniot elastic limit (HEL) of 3 GPa for Ta under 34 GPa of shock pressure. Lateral stress gauge measurements of shear strength by Gray et al.²³ extend up to shock stress of 12 GPa and report shear strengths of up to 3 GPa, in line with the high shear strengths reported here, albeit for lower pressures.

Other strength measurements in the 100-250 GPa pressure range have been performed using ramp loading, so that, again, there is a difference in strain rate compared to this work. Flow stress measurements of Ta ramp loaded to 1-2.5 Mbar have been performed through Rayleigh-Taylor instability measurements¹⁸ and wave-profile analysis²⁴. Both studies report flow stresses of $\sim 4-6$ GPa when ramp compressed to 1 Mbar, and Brown et al. observe the flow stress increases to 8-12 GPa for pressures of 2.2 Mbar²⁴. The flow stresses reported here, 3-4 times higher, are likely due to the higher strain rates associated with shock compression (10^5 s⁻¹ vs. 10^8 s⁻¹). In addition, the polycrystalline samples used in the ramp-compression studies may have additional deformation mechanisms available to relieve shear stress that are not active in these single-crystal experiments.

B. Strength Model

Two adaptations of the LMS model for strong shocks are shown in Fig. 7 (orange and blue curves). The plastic strain rate is used in the LMS model to set the dislocation density and dislocation velocity. We assume that the strain rate at the shock front will determine the dislocation density while the strain rate behind the shock front will set the dislocation velocity⁶. This view holds that strong shocks will generate dislocations in the shock front at the saturation level through homogeneous nucleation. The saturation dislocation density is determined from the plastic strain rate in the shock front, which is estimated using the Swegle-Grady relationship^{4,25}. The dislocations nucleated in the shock front are expected to persist in the material over the timescale of the experiment, similar to the behavior shown in Fig. 6 (B). For strong shocks, the shock front thickness is small and the bulk of the diffracting volume resides behind the shock front, implying that the flow stress observed in the Laue experiments will be related to the dislocation velocity behind the shock front. Hunter and Preston²⁶ asserted that the plastic strain rate will be zero behind the shock front for the purposes of model calculations. Simulations of the strain rate behind the shock front estimate that the strain rate can fall by a factor ~ 10 compared to the shock front,

but not necessarily to zero⁶. There is considerable uncertainty to the post-shock strain rate, and subsequently, we present the model estimates using the two extremes, assuming the plastic strain rate falls to zero behind the shock front or that the plastic strain rate stays equal to the shock front. The blue curve assumes the dislocation velocity based on Swegle-Grady strain rate^{4,6}, while the orange curve sets the dislocation velocity to zero, such that only the Taylor hardening contributes to the flow stress. The data above 100 GPa fall between these two bounding curves, consistent with strain rate greater than zero but lower than the shock front.

The dislocation density behind the shock front predicted by the LMS model is plotted in Fig. 7 (B) for shock strengths up to 65 GPa. Simple estimates using Orowan's law illustrate how the plastic strain rate observed in the Laue data can be used to infer the mobile dislocation density.

$$\rho_d = \frac{\dot{\epsilon}_p M}{b v_d \eta} \quad (5)$$

The plastic strain and subsequent strain rate can be found from the difference between the observed shear strain and the shear strain under uniaxial compression. For the data shown in Fig. 5, applying Eqs. (1) and (2) to the data gives a decrease in elastic strain of 0.05-0.07 over 0.2-0.6 ns, implying an average plastic strain rate of $0.8 - 4 \times 10^8 \text{ s}^{-1}$ during the relaxation phase. While both ρ_d and v_d are unknown, there is less uncertainty in v_d . v_d is widely assumed to be less than the shear wave speed (~ 2 - 2.5 km/s for Ta¹³), and MD simulations have predicted dislocation velocities of $\sim 700 \text{ m/s}$ for 10^8 strain rates²⁷. This is in general agreement with the LMS model, which predicts the dislocation velocity will fall from a peak of 600 m/s to near zero over the course of the relaxation phase, giving an average dislocation velocity $v_d = 300 \text{ m/s}$. For an average dislocation velocity of 300 m/s and $b = 2.86 \text{ \AA}$, this implies a dislocation density of $1 - 6 \times 10^{11} \text{ cm}^{-2}$. This range is plotted in Fig. 7, and agrees well with the LMS predicted dislocation density, $4.7 \times 10^{11} \text{ cm}^{-2}$, at 50 GPa. Lu et al.²⁸ and Hsiung et al.²⁹ both recovered single-crystal tantalum samples shock loaded to 45 GPa and observed dislocation densities of $1 \times 10^{11} \text{ cm}^{-2}$, although *ex-situ* measurements are expected to be lower than *in-situ* due to post-shock annealing. Figure 7 shows our experimentally inferred dislocation density, the LMS simulated dislocation density, and the *ex-situ* studies. Our simple calculation shows how the relaxation time implies a dislocation density on the order of magnitude seen both in recovered samples and the LMS model predictions.

Since we do not yet have the time resolution to measure relaxation times above 65 GPa, we estimate experimental upper bounds for dislocation density by equating the Taylor hardening stress to flow stress found from the Laue data.

$$\bar{\sigma} = G M b \beta \sqrt{\rho_d} \quad (6)$$

This method estimates an upper bound since it assumes the dislocation velocity is zero. We also show the results in Fig. 7 for approximating the dislocation density as the saturation density from the LMS model, assuming the Swegle-Grady strain rate for the shock front. Either way, these results suggest a large (1-2 orders of magnitude) increase in dislocation density as the shock strength is increased above $P_{thresh} \sim 65 \text{ GPa}$.

The large dislocation densities inferred from these experiments may be relevant to studies of the high pressure melting behavior of tantalum, where controversy over the apparent low melt temperatures observed in laser-heated diamond anvil cell experiments stand in contrast to melting found in shock wave experiments^{30,31}. Wu et al.³² suggested that one-dimensional plastic flow can create a partially disordered structure which appears BCC in most directions but glassy in the $\{110\}$ planes. The relationship between plasticity and melting has been previously included in melt models; Burakovsky et al.³³ asserted that the dislocation density at melt could be estimated by

$$\rho_d = \frac{0.6 \pm 0.2}{b^2} \quad (7)$$

which corresponds to $\rho_d \sim 7 \times 10^{14} \text{ cm}^{-2}$ for tantalum. While the dislocation densities inferred in this work for pressure above 65 GPa are significantly below the expected density at melt (~ 20 times smaller), it is possible they are consistent with a partially disorder structure, although Wu et al. do not estimate an equivalent dislocation density. Alternatively, Dewaele et al.³⁴ measured a higher melting curve that is consistent with shock experiments and attribute the previous, anomalously-low melt curve to either reactions between the Ta and the pressure medium or melting of the pressure medium.

C. Molecular Dynamics Simulations

MD simulations of single-crystal Ta shock compressed along the [001] direction provide widely varying responses depending on the inter-atomic potential used. Recent MD simulations of shock compressed tantalum using the Ravelo potential indicate dislocation densities can reach $2 - 6 \times 10^{13} \text{ cm}^{-2}$ for shock strengths of 20-60 GPa¹⁴. A similar result was obtained for simulations of copper shock compressed in the homogeneous nucleation regime, where Bringa et al.³⁵ obtained dislocation densities of $3 - 8 \times 10^{13} \text{ cm}^{-2}$. These dislocation densities are remarkably in line with the values shown in Fig. 7 when equating the measured shear stress to the Taylor hardening.

MD simulations using the extended Finnis-Sinclair (EFS) potential have indicated single-crystal Ta shock compressed along [001] direction can reach twin volume fractions of over 95%¹⁵. Twinning, while not incorporated into our analysis, cannot be completely ruled out by the current experiments. While the $\sim 1 \text{ ns}$ relaxation time observed for the 50 GPa is inconsistent with the

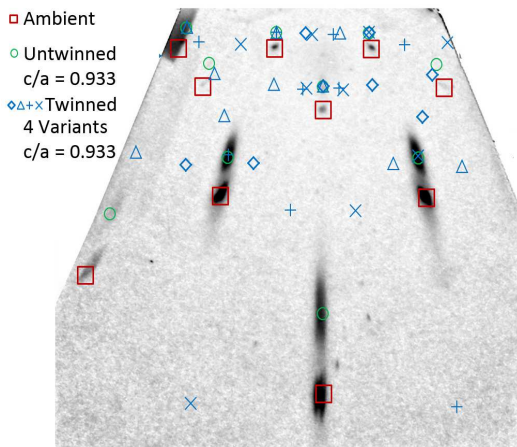


FIG. 8. Projection of Laue spots for the four variants of the $112 \langle 111 \rangle$ twinning mode onto Laue data for $[001]$ single-crystal Ta shock compressed to 64 GPa. Spots corresponding to the four variants are marked with blue symbols (\diamond , \triangle , $+$, and \times), while the ambient spots are marked with a red square and untwinned but uniaxially compressed spots are marked with a green circle. The twinned pattern overlaps many, but not all, of the untwinned spots.

short time scales, <100 ps, reported by Higginbotham et al.¹⁵, the transition to faster relaxation times above 65 GPa could indicate the onset of twinning. The dominant twinning mode (twin plane and direction) for BCC Ta is $\{112\} \langle 111 \rangle$ ¹⁵. Figure 8 projects Laue spots for the four twin variants of this mode onto the observed Laue data. The combination of the four variants overlaps many, although not all, of the Laue spots for the original untwinned lattice, but no spots corresponding only to a twin orientation were observed. For many shots, fewer driven Laue spots were observed, thus, while the data are not consistent with deformation by twinning only, a mixed twinning-slip deformation mechanism cannot be ruled out.

V. CONCLUSION

In-situ Laue diffraction was used to track the shear strain relaxation process of Ta single-crystals shocked along the $[001]$ direction. For shock strengths of 50 GPa, shear strain extends nearly to the uniaxial 1D elastic compression maximum and then relaxes to a near steady state over ~ 1 ns. At 80 and 125 GPa, uniaxial compression and relaxation are not observed even in the earliest data. This behavior is consistent with a transition to homogeneous nucleation of dislocations predicted by MD using the MGPT potential, allowing rapid relaxation on picosecond timescales. Based upon the relaxation rate and MD simulations of the dislocation velocity, a dislocation density of $1 - 6 \times 10^{11} \text{ cm}^{-2}$ is estimated for shocks of 50 GPa. The deduced dislocation densities jump by 1-2 orders of magnitude in crossing this predicted threshold at $P_{shk} \sim 65$ GPa. If one assumes the dislocation velocity falls to zero behind the shock front, dislocation densities of $4 \times 10^{13} \text{ cm}^{-2}$ can be estimated by equating the measured shear stress to the Taylor hardening rule, a value in line with dislocation densities found in MD simulations of shock compressed Ta¹⁴ and Cu³⁵. Twinning is also a mechanism that may be operative. While there is no evidence of twinning in the diffraction patterns, a mixed slip-twinning deformation mechanism cannot be ruled out by the current experiments.

VI. ACKNOWLEDGMENTS

This work was performed under the auspices of the U.S. Department of Energy by Lawrence Livermore National Security, LLC, Lawrence Livermore National Laboratory under Contract No. DE-AC52-07NA27344.

¹ B. Reed, R. Patterson, D. Swift, D. Stolken, R. Minich, and M. Kumar, J. Appl. Phys. **110**, 113506 (2011).

² D. Milathianaki, S. Boutet, G. J. Williams, A. Higginbotham, D. Ratner, A. E. Gleason, M. Messerschmidt, M. M. Seibert, D. C. Swift, P. Hering, J. Robinson, E. White, and J. S. Wark, Science **342**, 220 (2013).

³ N. R. Barton, J. V. Bernier, R. Becker, A. Arsenlis, R. Cavallo, J. Marian, M. Rhee, H.-S. Park, B. A. Remington, and R. T. Olson, J. Appl. Phys. **109**, 073501 (2011).

⁴ A. J. Comley, B. R. Maddox, R. E. Rudd, S. T. Prisbrey, J. A. Hawreliak, D. A. Orlikowski, S. C. Peterson, J. H. Satcher, A. J. Elsholz, H.-S. Park, B. A. Remington, N. Bazin, J. M. Foster, P. Graham, N. Park, P. A. Rosen, S. D. Rothman, A. Higginbotham, M. Suggit, and J. S. Wark, Phys. Rev. Lett. **110**, 115501 (2013).

⁵ R. E. Rudd, A. J. Comley, J. Hawreliak, B. R. Maddox, H. S. Park, and B. A. Remington, AIP Conf. Proc. **1426**,

1379 (2012).

⁶ A. J. Comley, B. R. Maddox, R. E. Rudd, N. R. Barton, C. E. Wehrenberg, S. T. Prisbrey, J. A. Hawreliak, D. A. Orlikowski, S. C. Peterson, J. H. Satcher, A. J. Elsholz, H.-S. Park, B. A. Remington, N. Bazin, J. M. Foster, P. Graham, N. Park, P. A. Rosen, S. D. Rothman, A. Higginbotham, M. Suggit, and J. S. Wark, Phys. Rev. Lett. **113**, 039602 (2014).

⁷ B. R. Maddox, H.-S. Park, B. A. Remington, C. Chen, S. Chen, S. T. Prisbrey, A. Comley, C. A. Back, C. Szabo, J. F. Seely, U. Feldman, L. T. Hudson, S. Seltzer, M. J. Haugh, and Z. Ali, Phys. Plasmas **18**, 056709 (2011).

⁸ C. Wehrenberg, A. J. Comley, R. E. Rudd, M. Terry, J. Hawreliak, B. R. Maddox, S. T. Prisbrey, H.-S. Park, and B. A. Remington, J. Phys. Conf. Series **500**, 112064 (2014).

- ⁹ P. M. Celliers, D. K. Bradley, G. W. Collins, D. G. Hicks, T. R. Boehly, and W. J. Armstrong, *Rev. Sci. Instr.* **75**, 4916 (2004).
- ¹⁰ D. E. Fratanduono, T. R. Boehly, P. M. Celliers, M. A. Barrios, J. H. Eggert, R. F. Smith, D. G. Hicks, G. W. Collins, and D. D. Meyerhofer, *J. Appl. Phys.* **110**, 073110 (2011).
- ¹¹ D. E. Fratanduono, (Oct 2013), private communication.
- ¹² D. E. Fratanduono, J. H. Eggert, M. C. Akin, R. Chau, and N. C. Holmes, *J. Appl. Phys.* **114**, 043518 (2013).
- ¹³ D. Orlikowski, P. Söderlind, and J. A. Moriarty, *Phys. Rev. B* **74**, 054109 (2006).
- ¹⁴ D. Tramontina, P. Erhart, T. Germann, J. Hawreliak, A. Higginbotham, N. Park, R. Ravelo, A. Stukowski, M. Suggit, Y. Tang, J. Wark, and E. Bringa, *High Energy Den. Phys.* **10**, 9 (2014).
- ¹⁵ A. Higginbotham, M. J. Suggit, E. M. Bringa, P. Erhart, J. A. Hawreliak, G. Mogni, N. Park, B. A. Remington, and J. S. Wark, *Phys. Rev. B* **88**, 104105 (2013).
- ¹⁶ G. Bazan, *Bull. Amer. Astron. Soc.* **31**, 669 (1999).
- ¹⁷ N. R. Barton and M. Rhee, *J. Appl. Phys.* **114**, 123507 (2013).
- ¹⁸ H. S. Park, R. E. Rudd, R. M. Cavallo, N. R. Barton, A. Arsenlis, J. L. Belof, K. J. M. Blobaum, B. S. El-dasher, J. N. Florando, C. M. Huntington, B. R. Maddox, M. J. May, C. Plechaty, S. T. Prisbrey, B. A. Remington, R. J. Wallace, C. E. Wehrenberg, M. J. Wilson, A. J. Comley, E. Giraldez, A. Nikroo, M. Farrell, G. Randall, and G. T. Gray III, *Phys. Rev. Lett.* **114**, 065502 (2015).
- ¹⁹ A. Dewaele and P. Loubeyre, *Phys. Rev. B* **72**, 134106 (2005).
- ²⁰ D. Antonangeli, D. L. Farber, A. H. Said, L. R. Benedetti, C. M. Aracne, A. Landa, P. Söderlind, and J. E. Klepeis, *Phys. Rev. B* **82**, 132101 (2010).
- ²¹ Q. Jing, Q. Wu, J. Xu, Y. Bi, L. Liu, S. Liu, Y. Zhang, and H. Geng, *J. Appl. Phys.* **117**, 055903 (2015).
- ²² M. Glam, M. Werdiger, Y. Horovitz, E. Moshe, and S. L. Pistinner, *J. Phys. Conf. Series* **500**, 112029 (2014).
- ²³ G. T. Gray, N. K. Bourne, and J. C. F. Millet, *J. Appl. Phys.* **94**, 6430 (2003).
- ²⁴ J. L. Brown, C. S. Alexander, J. R. Asay, T. J. Vogler, D. H. Dolan, and J. L. Belof, *J. Appl. Phys.* **115**, 043530 (2014).
- ²⁵ L. E. Murr, M. A. Meyers, C.-S. Niou, Y. J. Chen, S. Pappu, and C. Kennedy, *Acta Mater.* **45**, 157 (1996).
- ²⁶ A. Hunter and D. L. Preston, *Phys. Rev. Lett.* **113**, 039601 (2014).
- ²⁷ Y. Tang, E. M. Bringa, B. A. Remington, and M. A. Meyers, *Acta Mat.* **59**, 1354 (2011).
- ²⁸ C. H. Lu, B. A. Remington, B. R. Maddox, H. Park, S. T. Prisbrey, and M. A. Meyers, *Acta Mat.* **60**, 6601 (2013).
- ²⁹ L. L. Hsiung, *J. Phys.: Condens. Matter* **22**, 385702 (2010).
- ³⁰ D. Errandonea, M. Somayazulu, D. Häusermann, and H. K. Mao, *J. Phys.: Condens. Matter* **15**, 7635 (2003).
- ³¹ C. Dai, J. Hu, and H. Tan, *J. Appl. Phys.* **106**, 043519 (2009).
- ³² C. J. Wu, , P. Söderlind, J. Glosli, and J. E. Klepeis, *Nat. Mater.* **8**, 223 (2009).
- ³³ L. Burakovsky, D. L. Preston, and R. R. Silbar, *Phys. Rev. B* **61**, 15011 (2000).
- ³⁴ A. Dewaele, M. Mezouar, N. Guignot, and P. Loubeyre, *Phys. Rev. Lett.* **104**, 255701 (2010).
- ³⁵ E. M. Bringa, K. Rosolankova, R. E. Rudd, B. A. Remington, J. S. Wark, M. Duchaineau, D. H. Kalantar, J. Hawreliak, and J. Belak, *Nat. Mater.* **5**, 805 (2006).